Technical Report

Detecting creep transients in InSAR timeseries using deep neural networks

SCEC Award # 22077

Investigators: Roland Bürgmann (UCB), Yuexin Li (UCB), Gareth Funning (UCR)

Introduction and Motivation

Creeping faults in California exhibit both steady and episodic behaviors that consist of slow slip events (Wei et al., 2013). Growing evidence indicates that shallow fault creep can be triggered by nearby (e.g., Linde et al., 1996; Wei et al., 2011; Li & Bürgmann, 2021) or remote earthquakes (e.g., Tymofyeyeva et al., 2019), modulated by elevated pore pressure (Khoshmanesh et al., 2018), and composed of aseismic slip transients in addition to the background steady creep (e.g., Bilham & Behr, 1992; Rousset et al., 2016). Variable creep behaviors contribute to regional strain and stress variations, and accelerations of creep rates may produce stress perturbations on faults and even trigger earthquakes. Due to limited observations of such low-amplitude near-fault signals, the governing factors for variable creep behaviors are still not well understood. Better quantification of the spatiotemporal fault creep will not only reveal its underlying mechanisms but also provide insight for seismic hazard assessment.

Interferometric Synthetic Aperture Radar (InSAR) measures high-resolution large-scale ground deformation on a routine basis. With the launch of Sentinel-1, the satellite recurrence interval was reduced to 6-12 days globally, making it possible to monitor short-term transient deformation, such as afterslip (Wang & Burgmann, 2020), remotely triggered slow slip events (Tymofyeyeva et al., 2019), and shallow aseismic slip transients (Rousset et al., 2016). Theoretically, InSAR timeseries can reach sub-centimeter accuracy if the SBAS network is properly designed and atmospheric noise contributions are minimized (Ferretti et al., 2007). However, the detectability of the low amplitude transient signal is still largely limited by the contamination of atmospheric noises in SAR acquisitions.

Traditional atmospheric correction methods include applying an empirical model between topography and atmospheric delay (e.g., linear, Elliott et al., 2008; quadratic, Wright et al., 2004; power-law, Bekaert et al., 2015), using an external auxiliary dataset to estimate the atmospheric delay (e.g., Moderate Resolution Imaging Spectroradiometer, MODIS, Le et al., 2005; European Centre for Medium-Range Weather Forecasts, ECMWF, Jolivet et al., 2011; Generic Atmospheric Correction Online Service, GACOS, Yu et al., 2018), and applying stacking or temporal smoothing methods (e.g., common scene stacking, Tymofyeyeva and Fialko, 2015; Kalman filter, Dalaison and Jolivet, 2020). Even though the aforementioned methods have proven effective for long-term interseismic rate estimation, it is still challenging to extract low-amplitude transient signals from InSAR timeseries. Enabled by the increasing volume of SAR acquisitions, deep learning algorithms have been applied to automatically identify earthquake and volcano deformations in InSAR images (e.g., Anantrasirichai et al., 2018, 2019; Sun et al., 2020; Brengman & Barnhart, 2021). Moreover, Rouet-Leduc et al. (2021) developed an encoder-decoder neural network and showed its effectiveness in denoising InSAR timeseries.

In this study, we aim to develop a neural network structure that is well designed for detecting shallow creep transients, based on the encoder-decoder structure proposed by Rouet-Leduc et al. (2021). Specifically, we aim to evaluate a series of neural network structures trained with synthetic timeseries incorporating synthetic and real noise features, and finally apply the denoising method on the creeping North Anatolian Fault and Chaman Fault to identify transient

creep signals. The development of a successful InSAR denoising method will refine our understanding of how strain and stress evolve on continental creeping faults over time. This work also benefits past (e.g. ERS, Envisat, ALOS) and planned future SAR missions (e.g. NISAR) by mitigating the atmospheric delay in radar measurements.

Neural Network Structure

The autoencoder is a type of neural network that learns the key features of the input data and reconstructs the original input using its compressed representation. The denoising autoencoder (DAE) is one of its variations that adds noise into the original input and recovers the clean image through the encoder-decoder structure. The original introduction of DAE aimed to avoid overfitting and only learn robust features through deep neural networks. Currently, DAEs have been widely used in the image denoising community (e.g., applications in medical images, Gondara, 2016). We start with the autoencoder structure proposed by Rouet-Leduc et al. (2021) and modify the neural network design to optimize for the detection of transient fault creep events.

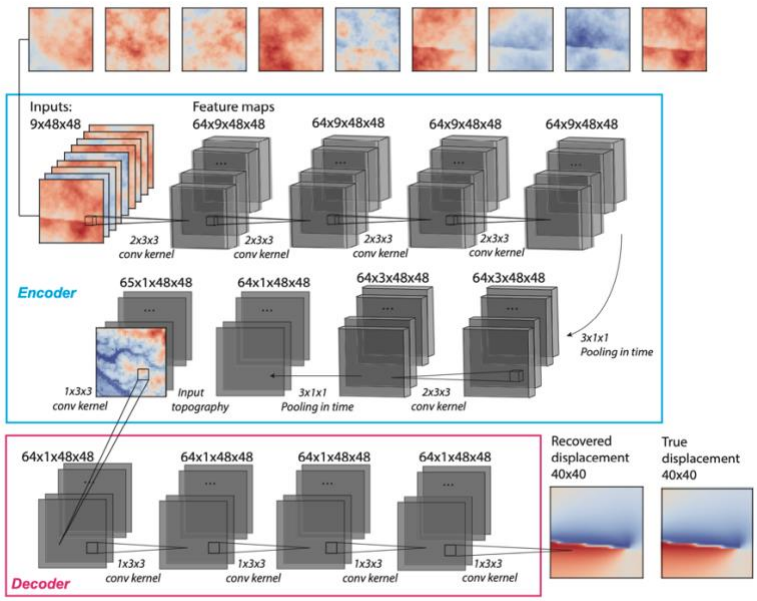

Figure 1: *The neural network structure of the denoising autoencoder that is adapted from Rouet-Leduc et al. (2021). It takes a batch of InSAR timeseries as input and outputs cumulative displacement over the same time period. A DEM is fed into the model as secondary input at the bottleneck.*

The detailed structure of the neural network adapted from Rouet-Leduc et al. (2021) is shown in Figure 1. The inputs of the DAE are a batch of InSAR timeseries consisting of 9 epochs. Through training, the DAE learns to differentiate between the spatiotemporal statistics of tectonic signal and atmospheric noise and output the noise-free cumulative displacement of the input timeseries. The DAE consists of 5 convolutional layers and 2 pooling layers in the encoder. Each pooling layer is reducing feature maps in the time domain, while keeping the spatial dimension unchanged. At the bottleneck, the topography is added as an extra feature map accounting for the topography-correlated atmospheric noises. A batch normalization layer is followed by the bottleneck. The DAE is further decoded with 4 convolutional layers to reconstruct the cleaned output. We use the rectified linear unit (ReLU) activation function after each convolutional layer.

Each convolutional layer contains 64 3x3x2 filter kernels in the encoder and 64 3×3×1 kernels in the decoder, respectively. In total, more than 400k trainable parameters are included.

Neural Network Training with Synthetic Datasets

The extraordinary number of trainable parameters in the DAE requires substantial training datasets to sufficiently train the neural network. Given there is no ground-truth noise-free measurements from InSAR, we will use synthetic deformation timeseries with added noises as training sets. For the spatial characteristics of the transient fault creep, we generate surface deformation through the Okada dislocation model (Okada, 1992), assuming an elastic homogeneous halfspace. Fault parameters including location, length, width, depth, strike, dip and the amount of strike-slip are randomly drawn from a uniform distribution within a given range. Here we constrain the fault depth to be close to the surface and the fault plane to be near vertical (70°-90°), representing behaviors of continental creeping faults. The 3D displacements are further projected into the line of sight (LOS) direction using randomly generated heading and incidence angle that are reasonable for Sentinel-1 ascending and descending viewing geometries.

For the generation of synthetic atmospheric noises, we assume the noises are composed of both spatial-correlated turbulence and topographic-correlated stratospheric delay. We simulate the spatially correlated Gaussian noise using the model proposed by Lohman & Simons (2005) and the topographic correlated noise model from Bekaert et al. (2015). For the topography-correlated tropospheric noise, the synthetic digital elevation models (DEMs) are randomly generated from isotropic 2D fractal surfaces with a power-law behavior (Hanssen, 2001).

The synthetic InSAR timeseries is generated by projecting the spatial characteristics of the deformation into a sequence following particular temporal evolution pattern. That is, the deformation signals share the same spatial pattern over time with evolving amplitudes. We assume the temporal evolution of the shallow creep transients follows the cumulative distribution function of a Gaussian distribution (Rouet-Leduc et al., 2021). The onset and end times of the transients are randomly generated as well. Under the assumption that the atmospheric perturbations are random in time, we add the atmospheric noise components to each epoch of the InSAR timeseries with a random signal-to-noise ratio (SNR) ranging from 10^{-5} to 10^{3}.

Evaluation on Synthetic Timeseries

The performance of the DAE strongly depends on the SNR of the input timeseries. We evaluate the performance of the trained DAE on synthetic InSAR timeseries with varying SNR (10^{-5}-10^{3}). We use the structural similarity index measure (SSIM), which is a matrix to evaluate similarity between images, as the accuracy of the neural network. SSIM=0 indicates a poor match between images, while SSIM=1 indicates a perfect match. An evaluation of the denoising accuracy (SSIM) with varying SNR is shown in Figure 2a. The trained DAE significantly improves the detection accuracy compared with timeseries analysis without correction.

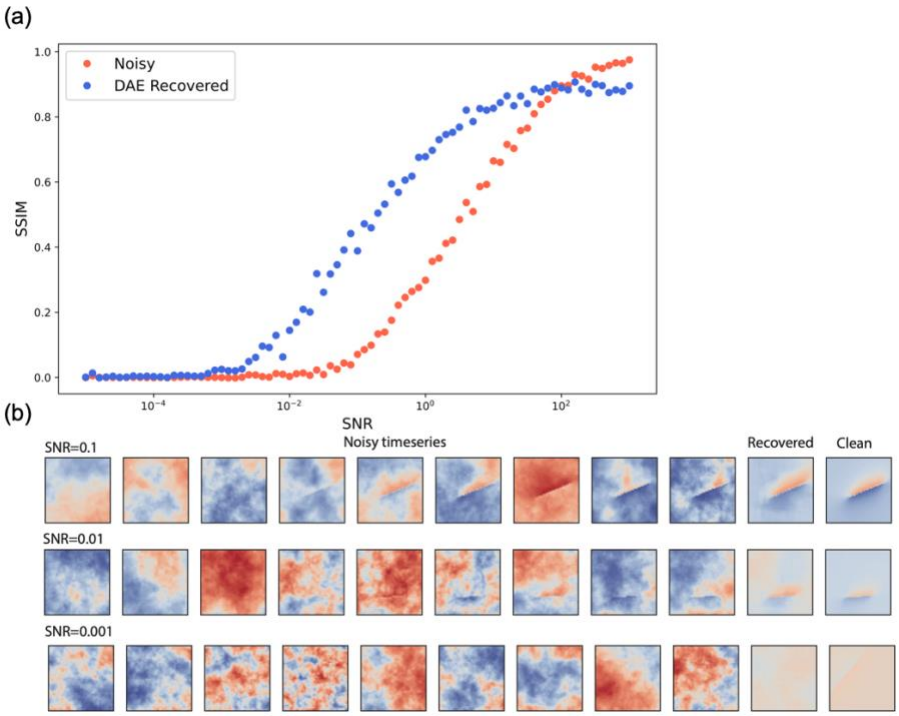

Figure 2: *(a) Performance of the denoising neural network model. Each point represents the average performance via the structural similarity index measure (SSIM) of a batch of InSAR timeseries for their corresponding SNR (batch size=64). The neural network model improves the detectability of timeseries analysis over a wide range of SNR (10^{-3}–10^{2}). (b) Examples of synthetic and DAE recovered InSAR cumulative displacement with SNR of 0.1, 0.01 and 0.001. The 1^{st}-9^{th} columns show the noisy InSAR timeseries, the 10^{th} column shows the DAE recovered cumulative displacement, and the last column shows the ground-truth noise-free displacement. The SSIM between recovered and noise-free cumulative displacements are 0.68, 0.16, and 0.03 for the timeseries with SNR of 0.1, 0.01, and 0.001, respectively.*

The DAE denoised timeseries show improved performance over a wide range of SNR (10^{3}-10^{2}). The DAE denoised timeseries achieve decent accuracy (SSIM=0.4) until SNR=0.1 whereas the noisy timeseries without denoising have an SSIM close to 0 and only reached the same accuracy with SNR=1. In general, the DAE enhances the detectability of shallow fault creep transient signals by at least 10 times. Figure 2b shows examples of synthetic noisy and DAE recovered InSAR timeseries and cumulative displacement with SNR of 0.1, 0.01, and 0.001. For low SNR InSAR timeseries (SNR<0.01, Figure 2b), more than 90% of the atmospheric noises are effectively removed regardless of the accuracy, suggesting the DAE's promising potential for both signal recovery and noise removal.

Evaluation on Real Timeseries

To further evaluate the performance of the DAE, we apply the trained neural network on InSAR timeseries on the North Anatolian Fault and the Chaman Fault. Both faults have segments exhibiting aseismic fault creep behaviors that are well-documented by InSAR observations (Cakir

et al., 2005; Kaneko et al., 2013; Cetin et al., 2014; Fattahi and Amelung, 2016; Rousset et al., 2016; Barnhart, 2017; Aslan et al., 2019; Dalaison et al., 2021).

The North Anatolian Fault

Located in northern Turkey, the 1200-km-long North Anatolian Fault (NAF) is the major active right-lateral fault accommodating the motion between the Anatolian and Eurasian plates at a rate of ~25 mm/yr (McClusky et al., 2000). Over the last decade, present-day deformation on the NAF has been well-documented by geodetic InSAR and GPS measurements (e.g., Cakir et al., 2005; Kaneko et al., 2013; Cetin et al., 2014; Rousset et al., 2016; Aslan et al., 2019; Weiss et al., 2020). At least two creeping sections have been identified on the NAF, including a 60-km-long section near the 1999 Mw7.6 Izmit earthquake rupture (Cakir et al., 2012) and the 80-km long Ismetpasa segment that hosts the 1944 Mw7.3 and 1951 Mw6.9 earthquakes (Cakir et al., 2012; Rousset et al., 2016). At the Ismetpasa creeping segment, Rousset et al. (2016) observes an aseismic transient slip episode using the timeseries analysis of the Cosmo-SkyMed (CSK) InSAR data between August-September 2013. The transient episode has ~2 cm of slip burst, which is equivalent to ~1 year of the tectonic loading (Rousset et al., 2016).

We test our trained DAE on the CSK timeseries from Rousset et al. (2016) spanning the period of the transient creep episode in 2013. Figure 3a-c shows the performance of the DAE on the timeseries on the NAF from 2013-09-06 to 2013-10-23. The atmospheric noises are effectively removed on the recovered cumulative displacement. The comparisons between fault-perpendicular velocity profiles (Figure 3c) show that the DAE is capable of removing the atmospheric noises over the region and enhancing the ability of InSAR to detect shallow fault creep.

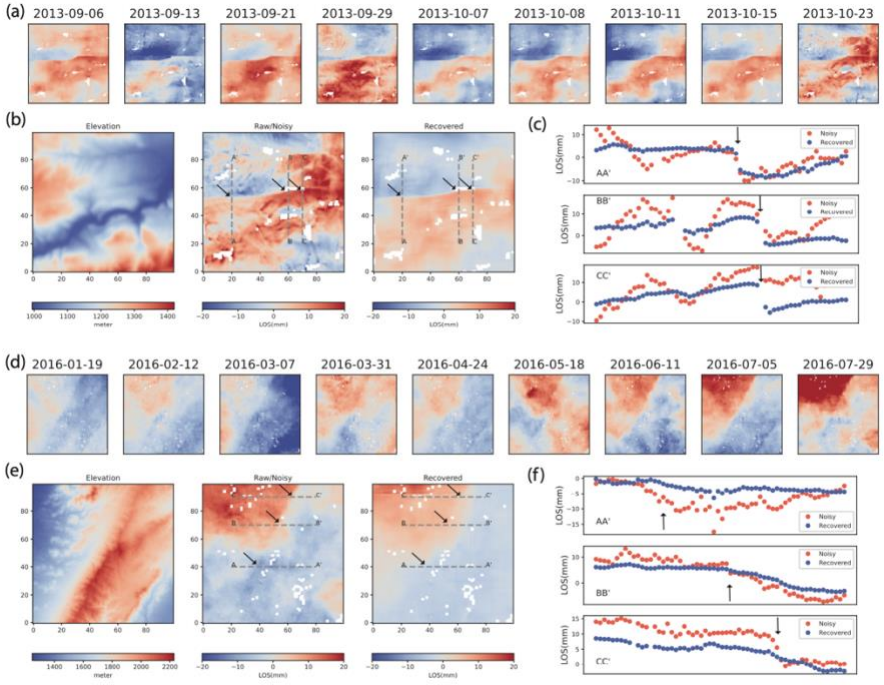

Figure 3: *Performance of the DAE neural network model on the (a-c) NAF and the (d-f) Chaman Fault. (a) Input CSK InSAR timeseries from Rousset et al. (2016). (b) Input DEM, original and DAE recovered cumulative displacement at the last scene (2013-10-23). (c) Comparisons of profiles between original and recovered displacement. Locations of profiles are labeled in (b). (d)Input Sentinel-1 InSAR timeseries from Kang Wang (pers. commun.). (e) Input DEM, original and DAE recovered cumulative displacement at the*

last scene (2016-07-29). (f) Comparisons of profiles between original and recovered displacement. Locations of profiles are labeled in (b).

The Chaman Fault

The ~1000-km-long Chaman fault zone in Afghanistan and Pakistan is the western boundary between India and Eurasia plates. At the complex transpressional plate boundary region, the tectonic plate motion is accommodated by both 23-36 mm/yr left-lateral strike-slip motion and 0-18 mm/yr convergence (DeMets et al., 2010; Kreemer et al., 2014; Dalaison et al., 2021). The Chaman Fault takes up ~30% of the strike-slip motion and slips at ~12 mm/yr (Dalaison et al., 2021). Spatially variable shallow fault creep has been identified on the Chaman Fault ranging from 0-12 mm/yr from InSAR observations (e.g., Fattahi and Amelung, 2016; Barnhart, 2017; Dalaison et al., 2021), accompanied by moderate size (M5-6) earthquakes along the fault.

For the Chaman Fault, we use the Sentinel-1 InSAR timeseries spanning 2015-2021 (Kang Wang, pers. commun.). Figure 3d-f shows the performance of the DAE on the timeseries on the Chaman Fault from 2016-01-19 to 2016-07-29. Again, the atmospheric noises are effectively removed from the cumulative displacement. However, we do not observe significant fault creep on the velocity profiles (Figure 3f). Note that the input Sentinel-1 timeseries are taken from a time period without known slow slip transients, and the approximately north-south geometry of the Chaman Fault also leads to only a small portion of the fault motion is being projected onto the InSAR LOS direction. It is possible that the SNR on the Chaman Fault is more than an order smaller than that observed on the east-west trending NAF during the transient episode. In addition, the steep topographic contrast along the Chaman Fault trace insert difficulties for the DAE to distinguish between fault creep signal and the topographic-correlated atmospheric noise.

Conclusion

We adopt the deep neural network structure called denoising autoencoder (DAE) from (Rouet-Leduc et al., 2021) and train the DAE using 10^6 synthetic InSAR timeseries with simulated spatially correlated and topographic-correlated atmospheric noises. The performance of the DAE is strongly dependent on the SNR of the input timeseries. The DAE show improved accuracy over a wide range of SNR (10^{-5}-10^3). We further evaluate the performance of the DAE on InSAR timeseries on the creeping North Anatolian Fault (NAF) and Chaman Fault. The DAE effectively removes atmospheric noises of the InSAR timeseries and recovers the creep transient episodes on the NAF. However, the creep signal on the Chaman Fault is not fully recovered. This is possibly due to the low SNR on the Chaman Fault creep and the steep topography co-located with the fault trace. The performance of the DAE can be further improved by incorporating InSAR timeseries with real noise taken from short-term interferograms using the transfer learning strategy.

References

Anantrasirichai, N. et al. (2018). "Application of Machine Learning to Classification of Volcanic Deformation in Routinely Generated InSAR Data". Journal of Geophysical Research: Solid Earth 123.8, pp. 6592–6606. doi: https://doi.org/10.1029/2018JB015911.

Anantrasirichai, N. et al. (2019). "The Application of Convolutional Neural Networks to Detect Slow, Sustained Deformation in InSAR Time Series". Geophysical Research Letters 46.21, pp. 11850–11858. doi: https://doi.org/10.1029/2019GL084993.

Aslan, G. et al. (2019). "Shallow Creep Along the 1999 Izmit Earthquake Rupture (Turkey)

From GPS and High Temporal Resolution Interferometric Synthetic Aperture Radar Data (2011–2017)". Journal of Geophysical Research: Solid Earth 124.2, pp. 2218–2236. issn: 21699356. doi: 10.1029/2018JB017022.

Barnhart, W. D. (2017). "Fault creep rates of the Chaman fault (Afghanistan and Pakistan) inferred from InSAR". Journal of Geophysical Research: Solid Earth 122.1, pp. 372–386. issn: 21699356. doi: 10.1002/2016JB013656.

Bekaert, D. P. S., A. Hooper, and T. J. Wright (2015). "A spatially variable power law tropospheric correction technique for InSAR data". Journal of Geophysical Research: Solid Earth 120.2, pp. 1345–1356. doi: https://doi.org/10.1002/2014JB011558.

Bilham, R. and J. Behr (June 1992). "A two-layer model for aseismic slip on the Superstition Hills fault, California". Bulletin of the Seismological Society of America 82.3, pp. 1223–1235. issn: 0037-1106. doi: 10.1785/BSSA0820031223.

Brengman, C. M. J. and W. D. Barnhart (2021). "Identification of Surface Deformation in InSAR Using Machine Learning". Geochemistry, Geophysics, Geosystems 22.3, e2020GC009204. doi: https://doi.org/10.1029/2020GC009204.

Cakir, Z. et al. (2005). "Creeping along the Ismetpasa section of the North Anatolian fault (Western Turkey): Rate and extent from InSAR". Earth and Planetary Science Letters. issn: 0012821X. doi: 10.1016/j.epsl.2005.06.044.

C¸akir, Z. et al. (2012). "Onset of aseismic creep on major strike-slip faults". Geology. issn: 00917613. doi: 10.1130/G33522.1.

Cetin, E. et al. (2014). "Extent and distribution of aseismic slip on the Ismetpasa segment of the North Anatolian Fault (Turkey) from Persistent Scatterer InSAR". Geochemistry, Geophysics, Geosystems. issn: 15252027. doi: 10.1002/2014GC005307.

Dalaison, M. and R. Jolivet (2020). "A Kalman Filter Time Series Analysis Method for InSAR". Journal of Geophysical Research: Solid Earth 125.7. e2019JB019150. doi: https://doi.org/10.1029/2019JB019150.

Dalaison, M. et al. (2021). "The Interplay Between Seismic and Aseismic Slip Along the Chaman Fault Illuminated by InSAR". Journal of Geophysical Research: Solid Earth e2021JB021935. doi: https://doi.org/10.1029/2021JB021935.

DeMets, C., R. G. Gordon, and D. F. Argus (2010). "Geologically current plate motions". Geophysical journal international 181.1, pp. 1–80. issn: 0956-540X.

Elliott, J. R. et al. (2008). "InSAR slip rate determination on the Altyn Tagh Fault, northern Tibet, in the presence of topographically correlated atmospheric delays". Geophysical Research Letters 35.12, n/a–n/a. issn: 0094-8276. doi: 10.1029/2008gl033659.

Fattahi, H. and F. Amelung (2016). "InSAR observations of strain accumulation and fault creep along the Chaman Fault system, Pakistan and Afghanistan". Geophysical Research Letters 43.16, pp. 8399–8406. issn: 19448007. doi: 10.1002/2016GL070121.

Ferretti, A. et al. (2007). "Submillimeter Accuracy of InSAR Time Series: Experimental Validation". IEEE Transactions on Geoscience and Remote Sensing 45.5, pp. 1142–1153. doi: 10.1109/TGRS.2007.894440.

Gondara, L. (2016). “Medical image denoising using convolutional denoising autoencoders”. In: 2016 IEEE 16th international conference on data mining workshops (ICDMW). IEEE, pp. 241–246. doi: doi:10.1109/ICDMW.2016.0041.

Hanssen, R. F. (2001). Radar interferometry: data interpretation and error analysis. Vol. 2. Springer Science & Business Media.

Jolivet, R et al. (2011). “Systematic InSAR tropospheric phase delay corrections from global meteorological reanalysis data”. Geophysical Research Letters 38.17. issn: 0094-8276. doi: https://doi.org/10.1029/2011GL048757.

Kaneko, Y. et al. (2013). “Interseismic deformation and creep along the central section of the North Anatolian Fault (Turkey): InSAR observations and implications for rate-and-state friction properties”. Journal of Geophysical Research: Solid Earth 118.1, pp. 316–331. issn: 21699356. doi: 10.1029/2012JB009661.

Khoshmanesh, M. and M. Shirzaei (2018). “Episodic creep events on the San Andreas Fault caused by pore pressure variations”. Nature Geoscience 11.8, pp. 610–614. issn: 17520908. doi: 10.1038/s41561-018-0160-2.

Kingma, D. P. and J. Ba (2014). “Adam: A method for stochastic optimization”. arXiv preprint arXiv:1412.6980.

Kreemer, C., G. Blewitt, and E. C. Klein (2014). “A geodetic plate motion and Global Strain Rate Model”. Geochemistry, Geophysics, Geosystems 15.10, pp. 3849–3889. issn: 1525-2027. doi: https://doi.org/10.1002/2014GC005407.

Li, Y. et al. (2021). “Heterogeneous Interseismic Coupling Along the Xianshuihe-Xiaojiang Fault System, Eastern Tibet”. Journal of Geophysical Research: Solid Earth 126.11, e2020JB021187. issn: 2169-9313. doi: https://doi.org/10.1029/2020JB021187.

Li, Y. and R. B ̈urgmann (2021). “Partial Coupling and Earthquake Potential Along the Xianshuihe Fault, China”. Journal of Geophysical Research: Solid Earth 126.7. issn: 2169-9313. doi: 10.1029/2020jb021406.

Li, Z. et al. (2005). “Interferometric synthetic aperture radar (InSAR) atmospheric correction: GPS, Moderate Resolution Imaging Spectroradiometer (MODIS), and InSAR integration”. Journal of Geophysical Research: Solid Earth 110.B3. doi: https://doi.org/10.1029/2004JB003446.

Linde, A. T. et al. (1996). “A slow earthquake sequence on the San Andreas fault”. Nature. issn: 00280836. doi: 10.1038/383065a0.

Lohman, R. B. and M. Simons (2005). “Some thoughts on the use of InSAR data to constrain models of surface deformation: Noise structure and data downsampling”. Geochemistry, Geophysics, Geosystems 6.1.

McClusky, S. et al. (2000). “Global Positioning System constraints on plate kinematics and dynamics in the eastern Mediterranean and Caucasus”. Journal of Geophysical Research: Solid Earth 105.B3, pp. 5695–5719. doi: https://doi.org/10.1029/1999JB900351.

Okada, Y. (1992). “Internal deformation due to shear and tensile faults in a half-space”. Bulletin - Seismological Society of America 82.2, pp. 1018–1040.

Paszke, A. et al. (2019). “PyTorch: An Imperative Style, High-Performance Deep Learning Library”. In: Advances in Neural Information Processing Systems 32. Curran Associates, Inc., pp. 8024–8035.

Rouet-Leduc, B. et al. (2021). “Autonomous extraction of millimeter-scale deformation in InSAR time series using deep learning”. Nature Communications 12.1, p. 6480. doi: 10.1038/s41467-021-26254-3. eprint: 2012.13849.

Rousset, B. et al. (2016). “An aseismic slip transient on the North Anatolian Fault”. Geophysical Research Letters. issn: 19448007. doi: 10.1002/2016GL068250.

Sengor, A. et al. (2005). “The North Anatolian fault: A new look”. Annu. Rev. Earth Planet. Sci. 33, pp. 37–112.

Sun, J. et al. (2020). “Automatic detection of volcanic surface deformation using deep learning”. Journal of Geophysical Research: Solid Earth 125.9, e2020JB019840.

Tong, X., D. T. Sandwell, and B. Smith-Konter (2013). “High-resolution interseismic velocity data along the San Andreas Fault from GPS and InSAR”. Journal of Geophysical Research: Solid Earth. issn: 21699356. doi: 10.1029/2012JB009442.

Tymofyeyeva, E. and Y. Fialko (2015). “Mitigation of atmospheric phase delays in InSAR data, with application to the eastern California shear zone”. Journal of Geophysical Research: Solid Earth 120.8, pp. 5952–5963. issn: 21699356. doi: 10.1002/2015JB011886.

Tymofyeyeva, E. et al. (2019). “Slow Slip Event On the Southern San Andreas Fault Triggered by the 2017 Mw8.2 Chiapas (Mexico) Earthquake”. Journal of Geophysical Research: Solid Earth 124.9, pp. 9956–9975. issn: 21699356. doi: 10.1029/2018JB016765.

Wang, K. and R. B ̈urgmann (2020). “Probing fault frictional properties during afterslip up and downdip of the 2017 Mw 7.3 Sarpol-e Zahab earthquake with space geodesy”. Journal of Geophysical Research: Solid Earth. issn: 2169-9313. doi: 10.1029/2020jb020319.

Wei, M. et al. (2011). “Slip on faults in the Imperial Valley triggered by the 4 April 2010 Mw 7.2 El Mayor-Cucapah earthquake revealed by InSAR”. Geophysical Research Letters 38.1.

Wei, M. et al. (2013). “Episodic fault creep events in California controlled by shallow frictional heterogeneity”. Nature geoscience 6.7, pp. 566–570.

Weiss, J. R. et al. (2020). “High-Resolution Surface Velocities and Strain for Anatolia From Sentinel-1 InSAR and GNSS Data”. Geophysical Research Letters 47.17. e2020GL087376 2020GL087376, e2020GL087376. doi: https://doi.org/10.1029/2020GL087376.

Wright, T. J. et al. (2004). “InSAR observations of low slip rates on the major faults of western Tibet”. Science 305.5681, pp. 236–239. issn: 00368075. doi: 10.1126/science.1096388.

Yu, C. et al. (2018). “Generic Atmospheric Correction Model for Interferometric Synthetic Aperture Radar Observations”. Journal of Geophysical Research: Solid Earth 123.10, pp. 9202–9222. doi: https://doi.org/10.1029/2017JB015305.